ACS APPLIED POLYMER MATERIALS

pubs.acs.org/acsapm Article

3D Printing of Functional Hydrogel Devices for Screenings of Membrane Permeability and Selectivity

Isabel Arias Ponce, Rahul Sujanani, Joshua D. Moon, Juan Manuel Urueña, Craig J. Hawker,* and Rachel A. Segalman*

Cite This: https://doi.org/10.1021/acsapm.4c02732 Read Online

ACCESS | Metrics & More | Article Recommendations | Supporting Information

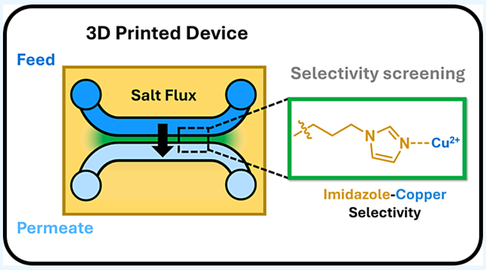

ABSTRACT: Developing a fundamental understanding of the effects of varying ligand chemistries on mass transport rates is key to designing membranes with solute-specific selectivity. While permeation cells offer a robust method to characterize membrane performance, they are limited to assessing a single membrane chemistry or salt solution per test. As a result, investigating the effects of varying ligand chemistries on membrane performance can be a tedious process, involving both the preparation of multiple samples and numerous, time-consuming permeation tests. This study uses digital light processing (DLP) 3D printing to fabricate a millifluidic flow-based permeation device made from a hydrogel active ester network that can be easily functionalized with ion-selective ligands. Without the need for bonding or assembly steps, ligands can be introduced and tested in the permeation device by simply injecting a small volume of a ligand solution. Various salt concentrations and molecular species can be cycled through a single device by switching the solution feeding into the salt reservoir, thereby reducing the number of samples needed for permeability and selectivity screenings. This research sets the groundwork for formulation development and postprocessing methods to 3D-print functional millifluidic devices capable of assessing solute selectivity in membranes and polymer adsorbents for aqueous separations. In this work, comparable salt permeability trends were observed with both 3D-printed devices and traditional assays. Devices were functionalized with an imidazole ligand to investigate salt permeability and selectivity of monovalent and divalent salts. Measurements showed increasing permeability for monovalent salts (NaCl) relative to divalent salts ($MgCl_2$, $CuCl_2$) in functionalized membranes, with higher monovalent/divalent selectivity at increasing imidazole grafting densities. The methods and findings described here represent a step toward developing higher-throughput methods with 3D-printed devices for screening the effects of ligand chemistry on mass transport rates in membrane materials.

KEYWORDS: *3D printing, millifluidics, permeability test, selectivity test, functionalization, ligand grafting, hydrogels*

1. INTRODUCTION

Many water treatment processes employ covalently cross-linked, hydrophilic polymer networks as nonporous membranes that separate ions from water.[1] Polymer networks functionalized with fixed charge groups (e.g., ion-exchange membranes or IEMs) are frequently applied in these processes due to their ability to reject similarly charged ions via Donnan exclusion, while selectively transporting ions of opposite charge.[1] While conventional IEMs achieve high salt rejection and selectivity between ions of opposite charge, selectivity between solutes of similar charge and size, which is required in emerging applications (e.g., resource recovery), remains a significant challenge for traditional membranes.[2−4] Recent studies have explored ion-selective sorption and transport in polymers functionalized with fixed ligand groups (e.g., crown-ethers, imidazoles, amines, and so forth) that can incorporate solute-specific interactions.[5−9] However, the design space for such materials is significant, and the effects of ligand density, binding strength, and water content on solute permeability and selectivity are often complex and intertwined. Thus, high-throughput experiments probing the influence of various ligand chemistries on solute transport rates are crucial for the more rapid development of design principles for solute-specific membranes.

Screening membrane properties across a wide variety of ligands presents inherent challenges because different synthetic routes can lead to changes in network structure and properties between samples, which makes direct comparisons challenging. Moreover, the preparation of reproducible membranes for successive tests introduces further variability. Previous work by Moon et al. addressed some of these challenges by developing a synthetic platform to systematically screen libraries of ligands via a pentafluorophenyl acrylate (PFPA) active ester group

Received: August 30, 2024
Revised: November 25, 2024
Accepted: November 25, 2024

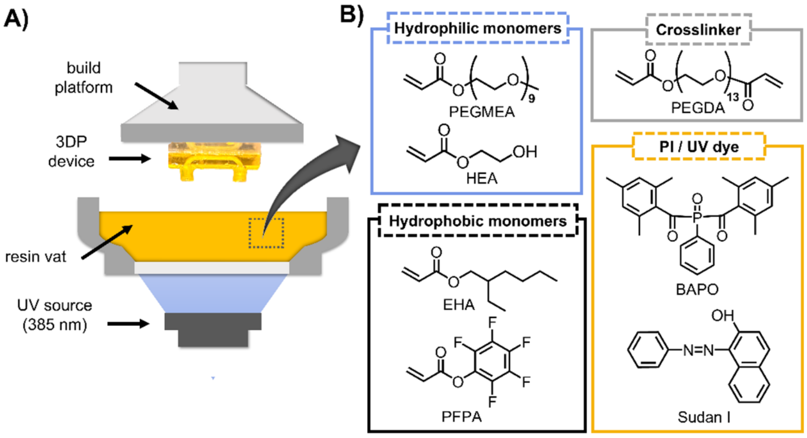

Figure 1. (A) Digital light processing (DLP) 3D printing was utilized to fabricate a functional, hydrogel-based permeation device. (B) Relevant chemical structures for the hydrophilic monomers, hydrophobic monomers (including the functional PFPA monomer), cross-linker, photoinitiator (PI), and UV dye used in our resin formulation. A high equilibrium water content was targeted for convenient transport detection while having a relatively small change in dimensional swelling during the solvent exchange to support high permeability rates while preserving print resolution. This was accomplished by tuning hydrophilic to hydrophobic comonomer ratios as well as prepolymerization solvent content.

substitution, by which basic, acidic, hydrophilic, hydrophobic, and solute-chelating moieties can be introduced.[7] This postfunctionalization approach allows for the same network structure and cross-link density to be studied, with the nature of the ligand being distinct from other correlated variables. This facilitates systematic screening of ligand chemistries for improved membrane performance. However, traditional membrane characterization strategies are still limited to a single sample per experiment. As a result, investigating chemistries for membrane separations can be a tedious process that involves reformulation of resins, preparation of multiple samples, and time-consuming transport experiments.

Permeability is a critical membrane property that characterizes concentration gradient-driven transport and is often measured using an established assay called the Franz diffusion cell or permeation cell.[10] A typical permeation cell consists of donor and receiver reservoirs secured around the membrane. While standard permeation cells offer a robust, well-established method to characterize transport across membranes, they have inherently low throughput since a single membrane structure and feed solution are measured per test. As a result, researchers in the membrane community have explored methods to more rapidly measure permeability. Kazemi et al. focused on a high-throughput technique to measure hydraulic filtration performance called stirred well filtration (SWF), which integrates 96-well plates, a multirack syringe pump, and individual pressure transducers to monitor the transmembrane pressure.[11] Another high-throughput approach developed by Muetzel et al. uses an automated device to rapidly characterize the hydraulic permeability and solute permeability of polymer membranes and assess how membrane chemistry affects concentration-dependent rejection profiles.[12] An alternative strategy to increase testing efficiency would be to utilize microfluidic devices, which are designed to miniaturize as well as parallelize tests by integrating channels at the microscale.[13] Some examples of microfluidic devices to measure transport include microfluidic skin-on-a-chip platforms for drug diffusion studies, freeform membranes anchored to microfluidics for permeation experiments, and patterned ion-selective hydrogels on microfluidics for desalination by electrodialysis.[14−16]

Vat photopolymerization, a light-based manufacturing process, that selectively cures liquid resin in a vat to build objects in a layer-by-layer fashion, has been increasingly used to fabricate microfluidic and millifluidic devices as it balances preparation time, resolution, and cost compared to traditional soft-lithography fabrication methods.[17] Vat photopolymerization includes both stereolithography (SLA) and digital light processing (DLP) techniques, which manufacture objects with either a laser or LED, respectively.[18] Various microfluidic devices have been fabricated via vat photopolymerization including a vascularized lung model for gas exchange, immunoaffinity monoliths for the detection of preterm birth biomarkers, and a multiwell microfluidic platform for drug testing of microdissected tissues.[19−21] These devices have been fabricated via vat photopolymerization to characterize membrane transport parameters such as diffusivity in hydrogel barriers, nanofiber membranes, and multimaterial porous channels.[22−24] However, the introduction of permeable structures within microfluidic chips typically requires intricate assembly and bonding steps or, in the case of multimaterial printing, vat-switching mechanisms and time-consuming cleanup between resin changes.

This study applies DLP 3D printing to fabricate millifluidic solute permeation devices composed of active ester hydrogel networks, which can be easily patterned with ion-selective ligands to screen their permeability and selectivity without additional assembly or reformulation steps. Resin optimization, device fabrication, and salt permeability measurements in unfunctionalized and ligand-grafted systems are presented. The device balances swelling-driven deformation in a semipermeable hydrogel network with suitable water volume fractions and tuned mechanical properties to withstand hours of testing. We demonstrate comparable permeability trends in both the 3D-printed devices and traditional permeation cells as well as increasing selectivity at higher imidazole grafting densities for monovalent salts (NaCl) over divalent salts ($MgCl_2$, $CuCl_2$). With simple changes to the printed geometry, multiple measurements could be carried out in parallel, and the effects of variations in membrane surface area and shape on permeability could be examined in future studies. This research lays the groundwork for higher-throughput ligand screenings of solute permeability and selectivity in membranes for water separations using a 3D-printed fluidic device made from an active ester hydrogel network.

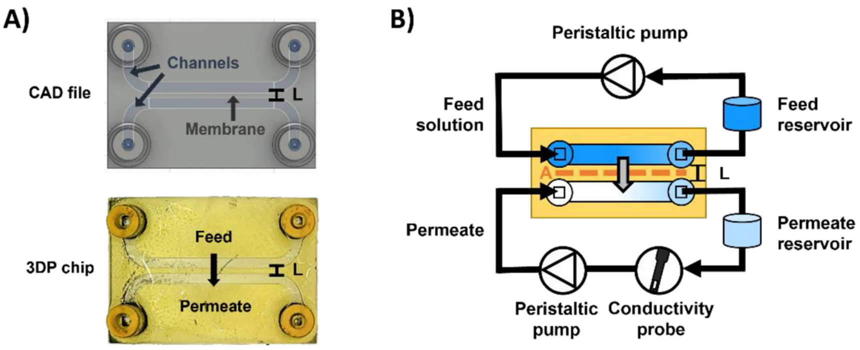

Figure 2. (A) Top view of the 3D printed functional permeation device, which contains two parallel channels (diameter 1 mm) separated by a thin membrane of thickness L (500 μm). (B) One channel circulates the feed solution (salt), and the second channel circulates the permeate solution (DI water) in parallel loops. Salt transport occurs down the concentration gradient across the semipermeable membrane. Increases in salt concentration in the permeate reservoir are monitored using a conductivity probe.

2. EXPERIMENTAL METHODS

2.1. Materials. Poly(ethylene glycol) methyl ether acrylate (PEGMEA M_n 480), ethylhexyl acrylate (EHA), poly(ethylene glycol) diacrylate (PEGDA M_W 700 kDa), phenylbis(2,4,6-trimethylbenzoyl)-phosphine oxide (BAPO), 1-phenylazo-2-naphthol (Sudan I), *dihydrolevoglucosenone* (Cyrene), sodium chloride (>99%), and copper(II) chloride (>99%) were purchased from Sigma-Aldrich. 2-Hydroxyethyl acrylate (HEA) and pentafluorophenyl acrylate (PFPA) were purchased from TCI America. Magnesium chloride hexahydrate (>98%) salt was purchased from Fisher Scientific. All chemicals were used as received.

2.2. Instrumentation. The permeation device was 3D-printed on a LumenX DLP printer (385 nm) from CELLINK in the BIOPACIFIC MIP user facilities at UC Santa Barbara. Membrane films for standard permeation tests were cured between quartz plates using an Analytik Jena UVA bulb (365 nm). The enclosure for fluidic connections was 3D-printed on a Formlabs Form 2 printer with Clear Resin V4. SF10 laboratory pumps from Vapourtec were used for the flow-based permeation studies. Conductivity measurements were carried out on an Orion Versa Star Pro pH/ISE/Conductivity Multiparameter Benchtop Meter with a Thermo Scientific Conductivity Probe. Salt calibration curves were generated for NaCl, $MgCl_2$, and $CuCl_2$ at room temperature. Fourier-transform infrared (FTIR) spectra were measured at room temperature on a Thermo Nicolet iS10 spectrometer with a Smart Diamond attenuated total reflectance (ATR) accessory using 64 scans.

2.3. Resin Development. A hydrogel composition was adapted from the work by Moon et al.[7] to prepare a 3D printable resin that could be functionalized postprinting. Resin components were tuned to achieve a 3D printable, semipermeable, and mechanically robust device with long-term shape fidelity in water (Figure 1A, Table S1). Nearly equal molar ratios of hydrophilic (PEGMEA, HEA) to hydrophobic (EHA, PFPA) monomers were used to minimize swelling-induced deformation of printed features. Introducing hydrophobic side groups onto the polymer network helped reduce polarity and control swelling without increasing the cross-linker density.[25] The cross-linker is also the main chemical parameter that controls gelation and printability as it leads to the formation of a random copolymer network structure upon light exposure and polymerization.[26] PFPA is an active ester acrylate monomer, which allows for quantitative functionalization of the network under mild conditions with a library of primary amines.[1] To fabricate a semipermeable device while minimizing swelling-driven deformation, a prepolymerization organic solvent (*dihydrolevoglucosenone,* Cyrene) was incorporated into the resin formulation (Tables S2 and S3). Cyrene, a biomass-derived sustainable solvent, was chosen due to its low volatility during the print process and high solubility to all resin components.[27] Increasing the amount of Cyrene from 0 to 24 and 48 wt % led to a decrease in swelling (eq S1) from 93 to 43 and 12%, respectively, while maintaining an equilibrium water volume fraction ϕ_w (eq S3) between 0.6 and 0.7 (Table S3). Detailed information on the methods used to measure swelling, water uptake, and water volume fractions can be found in section S2 of the SI. To generate resin formulations with increasing PFPA contents (0, 2, 5, 7 wt %) but similar water volume fractions (ϕ_w 0.6−0.7), the overall molar concentration of hydrophobic monomers was kept constant by lowering the EHA content (Tables S1 and S5). By using this methodology, an equilibrium water content typical of conventional water treatment IEMs was achieved while minimizing swelling-induced deformation. Swelling control was critical not only to preserve printed features but also to prevent gel brittleness and rupture, which are exacerbated during equilibration in water due to the development of internal stresses.[28] Following 3D printing, materials were thoroughly dialyzed to solvent-exchange Cyrene for water (Figure S2). Acetone was used as a dialysis solvent due to its high miscibility with all resin components and was sequentially switched to water through water-acetone mixtures (Table S2).

2.4. Device Design and Setup. The 3D-printed permeation device was designed to be a single-component, flow-based assay with parallel, rectangular feed and permeate channels separated by a semipermeable membrane of thickness *L* (Figure 2a). The chips had square channels with 1 mm height and 1 mm width as well as an interchannel membrane thickness of 500 μm (SI section 3, Figure S6). The chips were fabricated using a LumenX DLP 3D printer with print settings of 2 s per 50 μm layer at 50% UV power (7.09 mW/cm^2, manufacturer calibration) on a custom-made vat (Figure S1). The membrane shape and dimensions of the 3D printed device could be easily altered in the computer-assisted design (CAD) file (Figure S6).

Each channel was connected to a peristaltic pump, which independently recirculated the permeate and feed solutions through the 3D printed device in parallel closed loops (Figure 2b). Salt transport was explored in this study; therefore, aqueous salt solutions and initially pure deionized water were used as the feed and permeate reservoirs, respectively. Increases in salt concentration in the permeate channel due to salt diffusion from the feed channel were monitored at 30 s intervals using the conductivity probe at the permeate reservoir (Figure 2b).

2.5. Functionalization of 3DP Devices. Postfunctionalization of the semipermeable membrane between the feed and permeate channels for ion-ligand selectivity screenings was achieved via injection of 35 μL of a concentrated 45 wt % 1-(3-aminopropyl)-imidazole solution in dimethylformamide (DMF) into one channel (Figure 3a). The primary amine solution was in a molar excess of 1-(3-aminopropyl)imidazole relative to the pentafluorophenyl active ester group to ensure complete substitution and formation of the corresponding amide. Primary amine ligands functionalize channel-adjacent regions via passive reaction diffusion from the channel into the bulk of the gel, while distant regions remain unsubstituted. The substitution reaction occurs overnight at room temperature in a sealed jar to prevent evaporation of the primary amine solution. DMF was

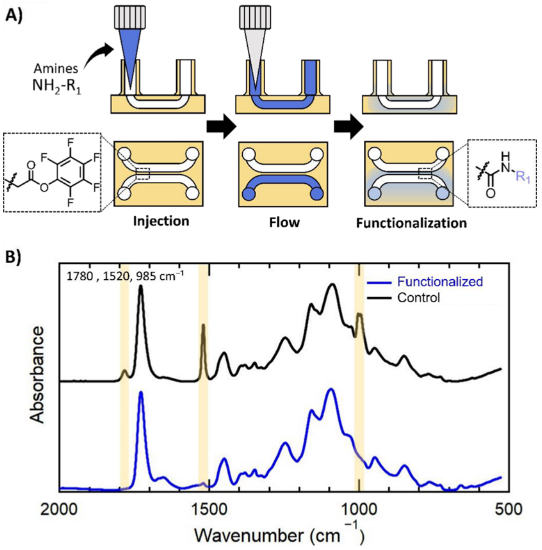

Figure 3. (A) Functionalization of the 3D printed permeation device occurs after the injection of a 1-(3-aminopropyl)imidazole solution and reaction-diffusion from the channel into the bulk of the hydrogel. (B) Upon functionalization, PFPA characteristic peaks disappear, and a characteristic amide peak appears in regions into which the amine has diffused and reacted.

chosen as the functionalization solvent due to its low volatility and low viscosity, which ensured high penetration of the ligand into the network and limited evaporation during the overnight reaction. Following substitution, the 3D-printed device was thoroughly dialyzed in acetone to remove any pentafluorophenol or unreacted imidazole from the network (SI section 1.5, Figure S3). Active ester substitution was confirmed by comparing the ATR-FTIR spectra of functionalized and unsubstituted regions. Upon functionalization, characteristic peaks for the pentafluorophenyl ester at 1780, 1520, and 985 cm^{-1} disappear, and characteristic peaks for the amide appear (i.e., 1160 cm^{-1}, Figure 3b), indicating efficient and quantitative substitution.

3. RESULTS AND DISCUSSION

3.1. Permeation Measurement with 3D Printed Device. Increases in permeate conductivity with time were correlated with increases in salt concentration via calibration curves generated for individual salts and probes. The salt flux (eq 1) was calculated by normalizing the change in permeate concentration with respect to time (dC/dt) by the active area of diffusion (A) and the total permeate volume (i.e., V_{permeate} = 60 mL). The active area of diffusion was approximated as the rectangular interface defined by the channel length and membrane height, which were measured using microscopy (Section S4.3). Salt flux determined in this manner can be used to calculate apparent permeability values by applying Fick's law at steady state for one-dimensional planar transport. This is a standard methodology to analyze concentration gradient-driven transport across films.[29,30] Based on this model, salt permeability values (eq 2) can be obtained by normalizing the salt flux by the membrane thickness L, measured via microscopy (Figure S9), and by the salt concentration difference between the feed and permeate reservoirs, ΔC.[31,32]

$$\text{Salt flux} = \frac{\mathrm{d}C}{\mathrm{d}t} \times \frac{V_{\text{permeate}}}{A} \tag{1}$$

$$\text{Permeability} = \frac{\mathrm{d}C}{\mathrm{d}t} \times \frac{V_{\text{permeate}}}{A} \times \frac{L}{\Delta C} \tag{2}$$

3.2. Demonstration of Salt Transport Measurements with 3D Printed Device. To demonstrate the capability of this device for measuring small molecule transport rates, we explored salt permeability in unfunctionalized resin formulations and compared these results to measurements using the traditional permeability assay. Traditional salt permeability experiments are static assays conducted in diffusion cells with two adjacent feed (salt) and permeate (water) chambers, separated by a semipermeable membrane. All three components are tightly clamped together, and salt transport occurs across the membrane down the concentration gradient (Figure 4a, left). The 3D printed permeation device contains all components within a single miniaturized chip, including feed and permeate channels as well as the semipermeable membrane between them (Figure 4a, right). Initially, NaCl permeability was measured using feed solutions of 0.01, 0.1, and 1 M (Figure 4b) since membrane studies frequently report the salt concentration dependence of various transport properties to model separation performance across different operation conditions.[33] Moreover, these concentrations are practically relevant in desalination, which treats low-salinity fresh water (≈ 2−10 g/L, ≈ 0.03−0.2 M) to high-salinity seawater (≈ 35 g/L, ≈ 0.6 M).[34] Since permeability values are related to flux normalized by the external concentration gradient (eq 2), permeability is expected to be relatively insensitive to changes in concentration for materials that exhibit weakly concentration-dependent solubilities and diffusivities. NaCl permeability measurements were observed to be essentially independent of concentration between 0.01 and 1 mol/L in both the traditional permeation assay and the 3D printed permeation device (Figure 4b). Different salts were also explored since the permeability of various molecular species is a commonly characterized performance metric. Furthermore, membrane separation efficiency is driven by the high permeation of one molecular species and the simultaneous low permeation of another, with the ratio of their permeabilities defined as the membrane selectivity between the salts.[35] Permeability measurements carried out with multiple salts of 1 M concentration also follow the same trends in both the traditional assay and the 3D printed permeation device, with the highest permeability for NaCl, intermediate permeability for $MgCl_2$, and lowest permeability for $CuCl_2$ (Figure 4c). The order of permeation observed between the various salts is consistent with the order of cation diffusivities in aqueous solution, which is inversely related to hydrated ion size. This behavior is expected, and typically observed, for ion transport in highly swollen membranes lacking ion-specific functionalities.[36,37] It is worth noting that all measurements shown in Figure 4, varying both salt concentrations (0.01, 0.1, and 1 M NaCl) and salt species (1 M NaCl, $MgCl_2$, and $CuCl_2$), were carried out in a single 3D printed device. The ability to change the salt tested by simply switching feed solutions instead of disassembling and reassembling a permeation cell is an advantage compared to the traditional method and offers increased testing throughput.

While similar trends are observed in both permeability assays, permeability values obtained from the 3D printed device are consistently higher than those obtained from the traditional assay by approximately a factor of 3 for all measurements. For the traditional permeability measurements, 500 μm membranes were cured between quartz plates by a UV mercury lamp by using the same resin applied to fabricate the 3D printed permeation device. Although the chemical

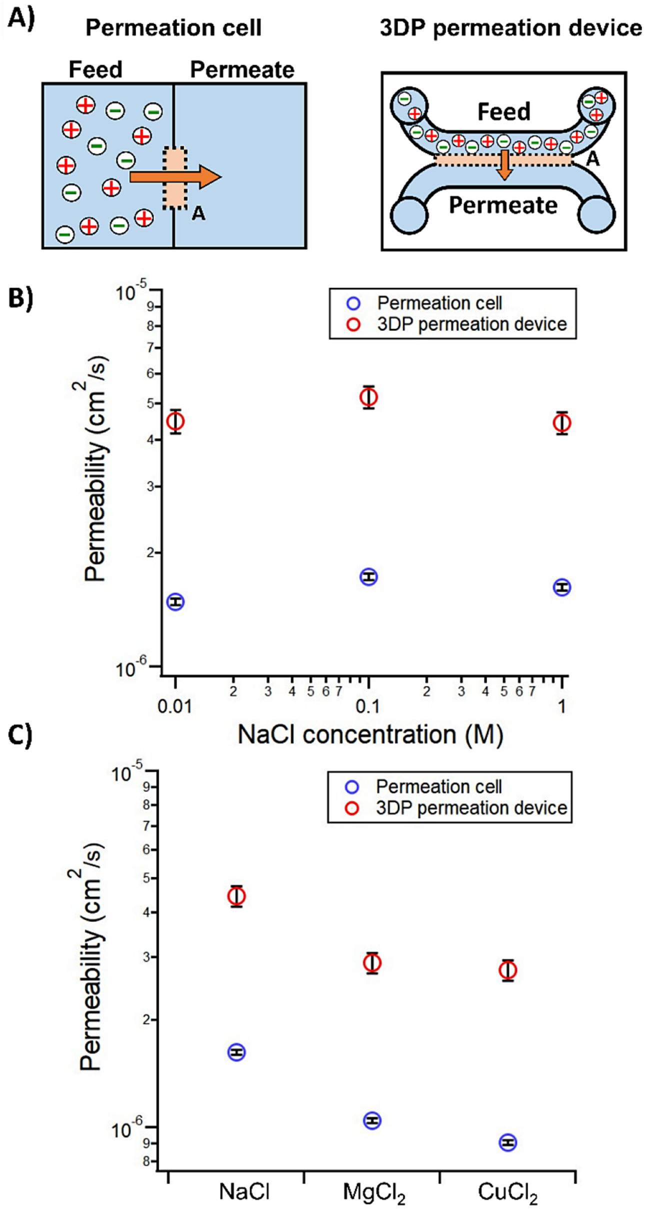

Figure 4. (A) Traditional permeability assays include permeate and feed chambers, a membrane secured between compartments, and a clamp to hold components together (left). The 3DP permeation device is a flow-based assay with a parallel feed and permeation channels separated by a thin membrane (right). (B) Permeability values are essentially independent of salt concentration for 0.01−1 M NaCl solutions with both the traditional assay and the 3DP permeation device. (C) Permeability measurements with various salts follow similar trends in both the 3DP permeation device and the traditional assay, with permeability values from highest to lowest: NaCl > $MgCl_2$ > $CuCl_2$. Permeability values from the 3DP permeation device are consistently higher than the traditional assay by a factor of 3, which is largely attributed to different fabrication methods leading to differences in water uptake. Error bars represent values calculated by a standard propagation of error analysis (SI section 4.5).

compositions of the resin formulation were identical, differences in permeability values could be attributed to the different fabrication methods. Membranes were cured as single films with a UV mercury lamp (365 nm), and devices were 3D printed in a layer-by-layer fashion with a UV LED (385 nm), leading to multiple interfaces. These differences in fabrication affect the extent of cross-linking, network structure, gel fraction, and water volume fraction. It is well-known that water content has a strong influence on salt solubility and diffusivity, and therefore salt permeability.[1] In general, membranes that sorb more water tend to have higher salt solubility and diffusivity, and both of these factors would increase salt permeability. Therefore, the lower gel fractions and higher water volume fractions observed for the 3D printed devices (gel fraction 0.7, ϕ_w 0.6) compared to the UV-cured membranes (gel fraction 0.9, ϕ_w 0.5) may explain the larger permeability values observed in the 3D printed devices (Table S4). Based on literature values of salt permeability versus water volume fraction for PEG-based membranes, we expect salt permeability to vary by about a factor of 2 due to the observed differences in the water volume fractions between the 3D printed and UV-cured materials[37] (SI Section 2.2, Figure S5). Moreover, conversion in vat-photopolymerized objects varies from a maximum value to one above the gelation threshold within each cured layer (50 μm thickness) due to a decay in light intensity governed by the Beer−Lambert absorption.[38] This inhomogeneity in chemical conversion could also contribute to the different permeability values between the traditional assay and the 3D printed device. A slightly larger area for mass transport in the 3D printed device than assumed in the simple 1D planar analysis that we employed could be another factor leading to higher permeability values. Given that the majority of salt transport is expected across the smallest distance between the channels (distance *L*) and the discrepancies between the 3D printed devices and thin-film membranes are largely attributed to differences in water uptake, a 1D planar analysis appears to be a reasonable first approximation. More intricate 3D transport analyses could be applied to relax this assumption, although transport trends and selectivity values should be independent of such geometrical factors. In general, the agreement observed between the permeability trends in both assays of varying salt concentrations and identities coupled with a constant factor between measurements demonstrates that the 3D printed device can be used to effectively screen salt transport behavior and trends in hydrogel materials.

3.3. Probing Ion-Ligand Selectivity with the 3D-Printed Permeation Device.

To show the capability of 3D printed permeation devices for screening ion-ligand selectivity, PFPA-containing chips were 3D printed, substituted with 1-(3-aminopropyl)imidazole, and single salt permeabilities of aqueous 0.1 M NaCl, $MgCl_2$, and $CuCl_2$ solutions were measured. 1-(3-Aminopropyl)imidazole was chosen as a control primary amine substituent for this study due to the strong coordination of azole-type ligands with divalent salts due to acid−base interactions.[39] Previous work by Moon et al. showed that the permeability of divalent salts (i.e., $MgCl_2$ and $CuCl_2$) decreased in imidazole-functionalized membranes relative to unfunctionalized membranes of similar water content. This decrease in permeability for divalent ions was attributed to strong ion-ligand interactions, which enhance salt partitioning but impede diffusion across the membrane.[7] On the other hand, the permeability of monovalent salts, such as sodium chloride, was far less affected by the presence of these functional groups within the network as the monovalent ions presumably do not interact strongly enough with the imidazole to affect sorption and diffusion in hydrated membranes. Within a few minutes of starting $CuCl_2$ permeability experiments with

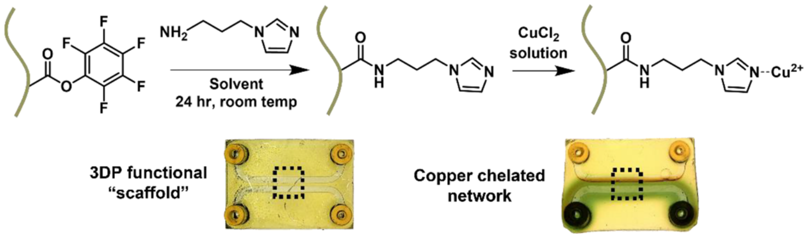

Figure 5. The 3D printed permeation device is made of a hydrogel network containing pentafluorophenyl active ester groups, which can be functionalized with 1-(3-aminopropyl)imidazole (top). Upon exposure to a copper chloride solution, copper cations strongly coordinate with imidazole groups functionalized within the network resulting in a characteristic green color change (bottom).

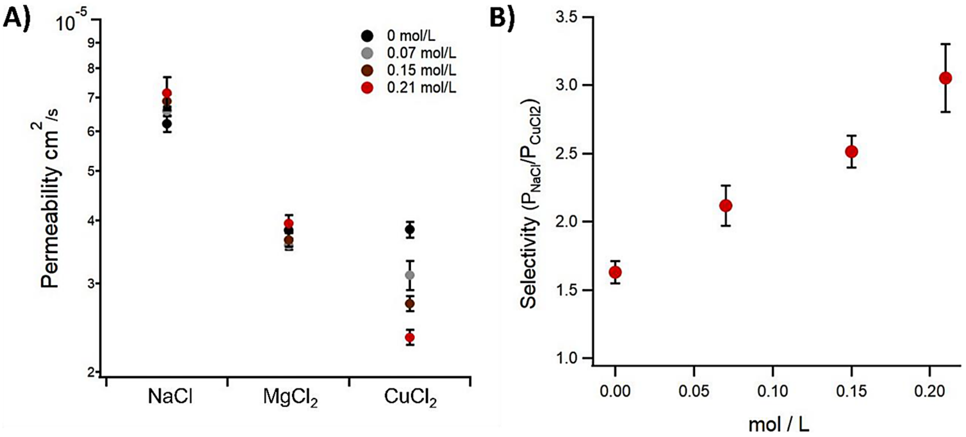

Figure 6. (A) 3DP permeation devices show decreasing permeability of $CuCl_2$ with increasing imidazole grafting densities (0, 0.07, 0.15, and 0.2 mol imidazole/L of swollen polymer). This is attributed to stronger copper-ligand interactions, which can hinder diffusion at higher ligand concentrations. For the other, noninteracting salts, NaCl and $MgCl_2$, permeability increased with increasing imidazole grafting densities due to increases in water volume fraction (Table S5). (B) Selectivity of imidazole-grafted materials increases with increasing ligand densities for $CuCl_2$ compared to NaCl. Error bars represent values calculated by a standard propagation of error analysis (SI section 4.5).

the 3D printed permeation device, copper-imidazole interactions could be visualized in the functionalized membranes as ligand-substituted regions surrounding the feed channel turned green upon exposure to the copper chloride solution and subsequent network chelation (Figure 5). It should be noted that unsubstituted membranes and 3D printed devices showed no change upon exposure to the copper chloride solution, which suggests no chelation/adsorption of Cu ions into the network (Figure S10b).

Besides qualitative observation of ion-ligand coordination via color change, the 3D-printed device was designed to probe ion-ligand selectivity as a function of imidazole grafting density through permeation measurements. To systematically analyze the effect of imidazole grafting density on salt permeability and selectivity, devices with different ligand concentrations were prepared using resin formulations with varied PFPA loadings (Table S1). Imidazole concentration is reported as moles of ligand per liter of the water-swollen membrane to account for the effect of the ligand on water sorption, which has a separate influence on salt permeability when compared to ion-ligand chelation.[7] Furthermore, normalizing by the volume of the swollen membrane accounts for how changes in water content either dilute or concentrate ligand density, which is relevant to modeling and interpreting mass transport in the presence of water.

$CuCl_2$ permeability decreased for the functionalized materials by a factor of 2 relative to the unfunctionalized materials at a grafting density of 0.21 mol imidazole/L of the swollen membrane (Figure 6a). This decrease in $CuCl_2$ permeability for imidazole-grafted membranes was also observed by Moon et al. due to strong imidazole-copper interactions. While previous work investigated a single imidazole density, this study showed that increasing ligand density continuously decreased $CuCl_2$ permeability. It is important to mention that increasing imidazole grafting densities also led to higher water uptake due to the hydrophilic nature of the imidazole ligand (Table S5). Increases in free volume due to higher water sorption typically increase salt permeability in swollen polymers lacking ion-specific interactions. This behavior was observed for NaCl transport in imidazole-functionalized membranes as NaCl permeability increased when imidazole concentration increased due to increased water content (Figure 6a).[7] On the other hand, $CuCl_2$ permeability values were lower than for NaCl and $MgCl_2$ at all imidazole-grafted densities and decreased with imidazole concentration, presumably due to strong copper-imidazole interactions that overwhelmed the effects of increased water sorption. This contrasts the permeability results in nongrafted materials, which are equivalent for divalent salts $MgCl_2$ and $CuCl_2$ (Figure 6a). The ideal selectivity values calculated from the single salt permeability ratio of NaCl and $CuCl_2$ (P_{NaCl}/P_{CuCl2}) also increased with an increasing imidazole concentration (Figure 6b). In future studies, multiple devices could be 3D printed in parallel and functionalized at varying concentrations of ligands to rapidly identify a ligand density and/or mixture that leads to a target or optimized selectivity.

4. CONCLUSIONS

This study details the design of a new method for screening salt permeability and selectivity of ligand-grafted membranes for water separation applications, using a flow-based 3D printed permeability device. Photochemically cured networks incorporating functional active ester chemistry were adapted to a 3D printable formulation and used to fabricate fluidic devices, which could be selectively functionalized with ligands such as 1-(3-aminopropyl)imidazole. The 3D printing resin was optimized to balance swelling-driven deformation, water volume fraction, and water uptake to yield a semipermeable material with shape fidelity of the printed features. Moreover, the hydrogel device demonstrated suitable mechanical properties to withstand processing steps, including ligand functionalization and solvent exchanges as well as hours of testing and cycling of feed and permeate solutions via peristaltic pumps. The fluidic permeation device was tested at varying salt concentrations and identities, with similar salt permeability trends being observed using the 3D printed device when compared to a traditional permeation assay. Similar measurements also showed increased permeability for monovalent salts (NaCl) relative to divalent salts ($MgCl_2$ and $CuCl_2$) for imidazole-functionalized membranes, with monovalent/divalent selectivity increasing as imidazole grafting density increased. The 3D-printed fluidic device could be used to screen multiple grafting densities, ligand chemistries, salt solutions, and salt concentrations via cycled experiments. By varying the design from two channels to multiple channels in parallel, the active ester chemistry could be leveraged in future studies to enable high-throughput ligand screenings of permeability and selectivity within a single device to identify promising polymer adsorbents. While these measurements are demonstrated for water separation applications, the methods developed here to fabricate a millifluidic device with an embedded permeable membrane could be extended to diverse fields including drug permeability testing and tissue permeation models.[40,41]

■ ASSOCIATED CONTENT

Supporting Information

The Supporting Information is available free of charge at https://pubs.acs.org/doi/10.1021/acsapm.4c02732.

> Experimental details, synthetic protocols, resin formulations, FTIR data, swelling/water uptake/water volume fraction data, and permeability/selectivity calculations and data (PDF)

■ AUTHOR INFORMATION

Corresponding Authors

Craig J. Hawker − *Materials Department and Department of Chemistry & Biochemistry, University of California Santa Barbara, Santa Barbara, California 93106, United States; Materials Research Laboratory, University of California Santa Barbara, Santa Barbara, California 93106-5121, United States;* orcid.org/0000-0001-9951-851X; Email: hawker@mrl.ucsb.edu

Rachel A. Segalman − *Materials Department, Department of Chemical Engineering, and Department of Chemistry & Biochemistry, University of California Santa Barbara, Santa Barbara, California 93106, United States; Materials Research Laboratory, University of California Santa Barbara, Santa Barbara, California 93106-5121, United States;* orcid.org/0000-0002-4292-5103; Email: segalman@ucsb.edu

Authors

Isabel Arias Ponce − *Materials Department, University of California Santa Barbara, Santa Barbara, California 93106, United States*

Rahul Sujanani − *Materials Department and Department of Chemical Engineering, University of California Santa Barbara, Santa Barbara, California 93106, United States*

Joshua D. Moon − *Materials Department and Department of Chemical Engineering, University of California Santa Barbara, Santa Barbara, California 93106, United States;* orcid.org/0000-0002-4402-2362

Juan Manuel Urueña − *National Science Foundation (NSF) BioPolymers, Automated Cellular Infrastructure, Flow, and Integrated Chemistry Materials Innovation Platform (BioPACIFIC MIP), University of California Santa Barbara, Santa Barbara, California 93106, United States*

Complete contact information is available at: https://pubs.acs.org/10.1021/acsapm.4c02732

Author Contributions

The manuscript was written through contributions of all authors. All authors have given approval to the final version of the manuscript.

Notes

The authors declare no competing financial interest.

Dryad datasets are available free of charge at https://doi.org/10.5061/dryad.ht76hdrr2.

■ ACKNOWLEDGMENTS

We gratefully acknowledge support from the Center for Materials for Water and Energy Systems (M-WET), an Energy Frontier Research Center funded by the U.S. Department of Energy, Office of Science, Basic Energy Sciences under Award #DE-SC0019272. We also made significant use of the facilities of the Materials Research Science and Engineering Center (MRSEC) at UC Santa Barbara: NSF DMR-2308708, which is a member of the Materials Research Facilities Network (www.mrfn.com), and of the facilities of the BIOPACIFIC Materials Innovation Platform (NSF 19-526) at UC Santa Barbara: NSF DMR-1933487. The authors also acknowledge the use of the Innovation Workshop within the California NanoSystems Institute, supported by the University of California, Santa Barbara and the University of California, Office of the President.

■ REFERENCES

(1) Geise, G. M.; Paul, D. R.; Freeman, B. D. Fundamental Water and Salt Transport Properties of Polymeric Materials. *Prog. Polym. Sci.* **2014**, *39* (1), 1−42.

(2) Sujanani, R.; Landsman, M. R.; Jiao, S.; Moon, J. D.; Shell, M. S.; Lawler, D. F.; Katz, L. E.; Freeman, B. D. Designing Solute-Tailored Selectivity in Membranes: Perspectives for Water Reuse and Resource Recovery. *ACS Macro Lett.* **2020**, *9* (11), 1709−1717.

(3) Epsztein, R.; DuChanois, R. M.; Ritt, C. L.; Noy, A.; Elimelech, M. Towards Single-Species Selectivity of Membranes with Subnanometre Pores. *Nat. Nanotechnol.* **2020**, *15* (6), 426−436.

(4) Kumarasamy, E.; Manning, I. M.; Collins, L. B.; Coronell, O.; Leibfarth, F. A. Ionic Fluorogels for Remediation of Per- and Polyfluorinated Alkyl Substances from Water. *ACS Cent. Sci.* **2020**, *6* (4), 487−492.

(5) Sepesy, M.; Fugate, B.; Duval, C. E. Amine-Functionalized Membrane Adsorbers to Purify Copper from Acidic Solutions. *ACS Appl. Polym. Mater.* **2022**, *4* (5), 3034−3044.

(6) Warnock, S. J.; Sujanani, R.; Zofchak, E. S.; Zhao, S.; Dilenschneider, T. J.; Hanson, K. G.; Mukherjee, S.; Ganesan, V.; Freeman, B. D.; Abu-Omar, M. M.; Bates, C. M. Engineering Li/Na Selectivity in 12-Crown-4−Functionalized Polymer Membranes. *Proc. Natl. Acad. Sci. U. S. A.* **2021**, *118* (37), No. e2022197118.

(7) Moon, J. D.; Sujanani, R.; Geng, Z.; Freeman, B. D.; Segalman, R. A.; Hawker, C. J. Versatile Synthetic Platform for Polymer Membrane Libraries Using Functional Networks. *Macromolecules* **2021**, *54* (2), 866−873.

(8) Nordness, O.; Moon, J. D.; Marioni, N.; Zofchak, E. S.; Richardson, P. M.; Landsman, M. R.; Katz, L. E.; Hawker, C. J.; Ganesan, V.; Segalman, R. A.; Clément, R. J. Probing Water and Ion Diffusion in Functional Hydrogel Membranes by PFG-NMR. *Macromolecules* **2023**, *56* (12), 4669−4680.

(9) Suresh, P.; Duval, C. E. Poly(Acid)-Functionalized Membranes to Sequester Uranium from Seawater. *Ind. Eng. Chem. Res.* **2020**, *59* (26), 12212−12222.

(10) Ng, S.-F.; Rouse, J. J.; Sanderson, F. D.; Meidan, V.; Eccleston, G. M. Validation of a Static Franz Diffusion Cell System for In Vitro Permeation Studies. *Aaps Pharmscitech* **2010**, *11* (3), 1432−1441.

(11) Kazemi, A. S.; Latulippe, D. R. Stirred Well Filtration (SWF)− A High-Throughput Technique for Downstream Bio-Processing. *J. Membr. Sci.* **2014**, *470*, 30−39.

(12) Muetzel, Z. W.; Ouimet, J. A.; Phillip, W. A. Device for the Acquisition of Dynamic Data Enables the Rapid Characterization of Polymer Membranes. *ACS Appl. Polym. Mater.* **2022**, *4* (5), 3438−3447.

(13) Mark, D.; Haeberle, S.; Roth, G.; von Stetten, F.; Zengerle, R. Microfluidic Lab-on-a-Chip Platforms: Requirements. *Characteristics and Applications. Chem. Soc. Rev.* **2010**, *39* (3), 1153−1182.

(14) Mohamadali, M.; Ghiaseddin, A.; Irani, S.; Amirkhani, M. A.; Dahmardehei, M. Design and Evaluation of a Skin-on-a-Chip Pumpless Microfluidic Device. *Sci. Rep.* **2023**, *13* (1), 8861.

(15) Hirschwald, L. T.; Brosch, S.; Linz, G.; Linkhorst, J.; Wessling, M. Freeform Membranes with Tunable Permeability in Microfluidics. *Adv. Mater. Technol.* **2023**, *8* (9), 2201857.

(16) Gumuscu, B.; Haase, A. S.; Benneker, A. M.; Hempenius, M. A.; van den Berg, A.; Lammertink, R. G. H.; Eijkel, J. C. T. Desalination by Electrodialysis Using a Stack of Patterned Ion-Selective Hydrogels on a Microfluidic Device. *Adv. Funct. Mater.* **2016**, *26* (47), 8685−8693.

(17) Weisgrab, G.; Ovsianikov, A.; Costa, P. F. Functional 3D Printing for Microfluidic Chips. *Adv. Mater. Technologies* **2019**, *4* (10), No. 1900275.

(18) Milton, L. A.; Viglione, M. S.; Ong, L. J. Y.; Nordin, G. P.; Toh, Y.-C. Vat Photopolymerization 3D Printed Microfluidic Devices for Organ-on-a-Chip Applications. *Lab a Chip* **2023**, *23* (16), 3537−3560.

(19) Grigoryan, B.; Paulsen, S. J.; Corbett, D. C.; Sazer, D. W.; Fortin, C. L.; Zaita, A. J.; Greenfield, P. T.; Calafat, N. J.; Gounley, J. P.; Ta, A. H.; Johansson, F.; Randles, A.; Rosenkrantz, J. E.; Louis-Rosenberg, J. D.; Galie, P. A.; Stevens, K. R.; Miller, J. S. Multivascular Networks and Functional Intravascular Topologies within Biocompatible Hydrogels. *Science* **2019**, *364* (6439), 458−464.

(20) Almughamsi, H. M.; Howell, M. K.; Parry, S. R.; Esene, J. E.; Nielsen, J. B.; Nordin, G. P.; Woolley, A. T. Immunoaffinity Monoliths for Multiplexed Extraction of Preterm Birth Biomarkers from Human Blood Serum in 3D Printed Microfluidic Devices. *Anal.* **2022**, *147* (4), 734−743.

(21) Horowitz, L. F.; Rodriguez, A. D.; Au-Yeung, A.; Bishop, K. W.; Barner, L. A.; Mishra, G.; Raman, A.; Delgado, P.; Liu, J. T. C.; Gujral, T. S.; Mehrabi, M.; Yang, M.; Pierce, R. H.; Folch, A. Microdissected "Cuboids" for Microfluidic Drug Testing of Intact Tissues. *Lab a Chip* **2021**, *21* (1), 122−142.

(22) Kim, Y. T.; Bohjanen, S.; Bhattacharjee, N.; Folch, A. Partitioning of Hydrogels in 3D-Printed Microchannels. *Lab a Chip* **2019**, *19* (18), 3086−3093.

(23) Choi, J. W.; Lee, J.; Yang, J.; Kim, Y. W.; Park, S. H.; Kim, S.; Hong, S.; Son, Y.; Han, J.; Ha, C. W. A Three-Dimensional Liquid-Based Exchangeable Gradient Osmosis Chip for a Permeability Controllable Microfluidic Device. *ACS Appl. Polym. Mater.* **2021**, *3* (11), 5836−5844.

(24) Kim, Y. T.; Castro, K.; Bhattacharjee, N.; Folch, A. Digital Manufacturing of Selective Porous Barriers in Microchannels Using Multi-Material Stereolithography. *Micromachines* **2018**, *9* (3), 125.

(25) Zhan, Y.; Fu, W.; Xing, Y.; Ma, X.; Chen, C. Advances in Versatile Anti-Swelling Polymer Hydrogels. *Mater. Sci. Eng.: C* **2021**, *127*, No. 112208.

(26) Schwartz, J. J. Additive Manufacturing: Frameworks for Chemical Understanding and Advancement in Vat Photopolymerization. *MRS Bull.* **2022**, *47*, 628−641.

(27) Stini, N. A.; Gkizis, P. L.; Kokotos, C. G. Cyrene: A Bio-Based Novel and Sustainable Solvent for Organic Synthesis. *Green Chem.* **2022**, *24* (17), 6435−6449.

(28) Leslie, K.-A.; Doane-Solomon, R.; Arora, S.; Curley, S. J.; Szczepanski, C.; Driscoll, M. M. Gel Rupture during Dynamic Swelling. *Soft Matter* **2021**, *17* (6), 1513−1520.

(29) Wijmans, J. G.; Baker, R. W. The Solution-Diffusion Model: A Review. *J. Membr. Sci.* **1995**, *107* (1−2), 1−21.

(30) Paul, D. R. Reformulation of the Solution-Diffusion Theory of Reverse Osmosis. *J. Membr. Sci.* **2004**, *241* (2), 371−386.

(31) Lonsdale, H. K.; Merten, U.; Riley, R. L. Transport Properties of Cellulose Acetate Osmotic Membranes. *J. Appl. Polym. Sci.* **1965**, *9* (4), 1341−1362.

(32) Geise, G. M.; Freeman, B. D.; Paul, D. R. Characterization of a Sulfonated Pentablock Copolymer for Desalination Applications. *Polymer* **2010**, *51* (24), 5815−5822.

(33) Wang, L.; Cao, T.; Dykstra, J. E.; Porada, S.; Biesheuvel, P. M.; Elimelech, M. Salt and Water Transport in Reverse Osmosis Membranes: Beyond the Solution-Diffusion Model. *Environ. Sci. Technol.* **2021**, *55* (24), 16665−16675.

(34) Ebrahim, M. A.; Karan, S.; Livingston, A. G. On the Influence of Salt Concentration on the Transport Properties of Reverse Osmosis Membranes in High Pressure and High Recovery Desalination. *J. Membr. Sci.* **2020**, *594*, No. 117339.

(35) Park, H. B.; Kamcev, J.; Robeson, L. M.; Elimelech, M.; Freeman, B. D. Maximizing the Right Stuff: The Trade-off between Membrane Permeability and Selectivity. *Science* **2017**, *356* (6343), 1138−1148.

(36) Stenina, I. A.; Yaroslavtsev, A. B. Ionic Mobility in Ion-Exchange Membranes. *Membranes* **2021**, *11* (3), 198.

(37) Ju, H.; Sagle, A. C.; Freeman, B. D.; Mardel, J. I.; Hill, A. J. Characterization of Sodium Chloride and Water Transport in Crosslinked Poly(Ethylene Oxide) Hydrogels. *J. Membr. Sci.* **2010**, *358* (1−2), 131−141.

(38) Uzcategui, A. C.; Higgins, C. I.; Hergert, J. E.; Tomaschke, A. E.; Crespo-Cuevas, V.; Ferguson, V. L.; Bryant, S. J.; McLeod, R. R.; Killgore, J. P. Microscale Photopatterning of Through-Thickness Modulus in a Monolithic and Functionally Graded 3D-Printed Part. *Small Sci.* **2021**, *1* (3), No. 2000017.

(39) Trojer, M. A.; Movahedi, A.; Blanck, H.; Nydén, M. Imidazole and Triazole Coordination Chemistry for Antifouling Coatings. *J. Chem* **2013**, *2013*, No. 946739.

(40) Zhu, C.; Jiang, L.; Chen, T.-M.; Hwang, K.-K. A Comparative Study of Artificial Membrane Permeability Assay for High Throughput Profiling of Drug Absorption Potential. *Eur. J. Med. Chem.* **2002**, *37* (5), 399−407.

(41) Azizgolshani, H.; Coppeta, J. R.; Vedula, E. M.; Marr, E. E.; Cain, B. P.; Luu, R. J.; Lech, M. P.; Kann, S. H.; Mulhern, T. J.; Tandon, V.; Tan, K.; Haroutunian, N. J.; Keegan, P.; Rogers, M.; Gard, A. L.; Baldwin, K. B.; de Souza, J. C.; Hoefler, B. C.; Bale, S. S.; Kratchman, L. B.; Zorn, A.; Patterson, A.; Kim, E. S.; Petrie, T. A.; Wiellette, E. L.; Williams, C.; Isenberg, B. C.; Charest, J. L. High-

Throughput Organ-on-Chip Platform with Integrated Programmable Fluid Flow and Real-Time Sensing for Complex Tissue Models in Drug Development Workflows. *Lab Chip* **2021**, *21* (8), 1454−1474.